Shekhawat, Deepshikha; Sulman, Muhammad; Flock, Dominik; Ecke, Gernot; Glaser, Marcus; Döll, Joachim; Bergmann, Jean Pierre; Pezoldt, Jörg

Controlling the reaction path of Ni/Al reactive multilayer on substrates

Original published in:	Journal of alloys and compounds : JAL ; an interdisciplinary journal of materials science and solid-state chemistry and physics. - Lausanne : Elsevier, 1010 (2025), art. 178026, 11 pp.
Original published:	2024-12-10
ISSN:	0925-8388
DOI:	10.1016/j.jallcom.2024.178026
[*Visited:*	2025-04-14]

Journal of Alloys and Compounds 1010 (2025) 178026

Contents lists available at ScienceDirect

Journal of Alloys and Compounds

journal homepage: www.elsevier.com/locate/jalcom

Controlling the reaction path of Ni/Al reactive multilayer on substrates

Deepshikha Shekhawat [a,*], Muhammad Sulman [a], Dominik Flock [b], Gernot Ecke [a], Marcus Glaser [c], Joachim Döll [d], Jean Pierre Bergmann [c], Jörg Pezoldt [a]

[a] FG Nanotechnologie, Institut für Mikro, und Nanolektronik and Institut für Mikro, und Nanotechnologien MacroNano® and Institut für Werkstofftechnik, Fakultät für Elektrotechnik und Informationstechnik, TU Ilmenau, Gustav-Kirchhoff-Straße 7, Ilmenau 98684, Germany
[b] FG Werkstoffe der Elektrotechnik, Institut für Werkstofftechnik and Institut für Mikro, und Nanolektronik and Institut für Mikro, und Nanotechnologien MacroNano®, Fakultät für Elektrotechnik und Informationstechnik, TU Ilmenau, Gustav-Kirchhoff-Straße 5, Ilmenau 98693, Germany
[c] FG Fertigungstechnik, Institut für Mikro, und Nanotechnologie MacroNano® and Institut für Mobilitätsforschung, Fakultät für Maschinenbau, Technische Universität Ilmenau, Gustav-Kirchhoff-Platz 2, Ilmenau 98693, Germany
[d] Zentrum für Mikro, und Nanotechnologien, TU Ilmenau, Gustav-Kirchhoff-Straße 7, Ilmenau 98684, Germany

ARTICLE INFO

Keywords:
Reactive multilayers
Self-sustained reaction
Nickel
Aluminum
Propagation velocity
Phase transformation
Reaction path shaping

ABSTRACT

In this study, we explore the transferability of the exothermic reaction between structured Ni/Al multilayers elements. Two systems were prepared with and without Sn as an adhesive layer between substrates and multilayers to investigate the effect on the reaction front. To achieve this, obstacles of varying sizes were integrated into Ni/Al multilayer foils using a combination of photolithography and lift-off techniques. They were systematically positioned along the path of the self-sustained reaction in Ni/Al multilayers on substrates, with different spacing configurations between them. The advancement of the reaction front was monitored using a high-speed camera, while time-resolved pyrometer measurements provided insights into the maximum temperature attained during the self-propagating reaction. X-ray diffraction analysis confirmed the formation of the NiAl phase formed in both systems, while scanning electron microscopy revealed morphological changes induced by the reaction in both the Ni/Al multilayers and the quenching zone. Notably, the reaction front halted at various intervals between obstacles. Our findings suggest several key observations: (I) Minimal spacing between obstacles can effectively quench the reaction front; (II) The modification of the heat loss by the adhesive layer and subsequently impacts the reaction front; (III) To determine the condition to tailor the heat release of the reactive Ni/Al multilayer systems; (IV) The observation revealed that Sn initiates compressive stress during the deposition of the Ni/Al multilayers. Additionally, it aids in decreasing the cooling rate after the reaction and facilitates grain growth in the Ni/Al multilayers afterward.

1. Introduction

Ni/Al reactive materials are characterized by the possibility of initiating a self-sustaining exothermic reaction to form intermetallic alloys [1,2]. Nanostructured intermetallic aluminide compounds exemplify this, with properties like low density, high wear resistance, hardness, strength, creep resistance, and oxidation resistance at elevated temperatures [3]. A self-propagating reaction is initiated when local mixing releases enough thermal energy to heat surrounding material, creating a reaction front that moves through the material at a particular velocity. Reactive multilayers are used as heat sources for bonding [4,5], igniters [6,7], thermal batteries [8], as well as in PyroMEMS [9], micropyrotechnics [10], and shape memory applications [11]. Several methods have been explored to fabricate solid-solid reactive materials, including powder mixtures [12,13], reactive multilayers [14,15], core-shell particle systems [16,17], particulate multilayers [18], and reactive multilayer particulate systems [19]. Techniques to produce aluminides from elemental constituents include cold rolling and annealing [20], high-pressure torsion with thermal processing [3], ball milling for mechanical alloying [21], liquid-phase casting [22], ion beam mixing of Ni/Al multilayers [23], and physical vapour deposition (PVD) based multilayer formation [1]. Phase formation in the Ni/Al system is typically influenced by the Al-Ni ratio and processing temperature, as predicted by the equilibrium phase diagram, assuming sufficient atomic mobility and interaction time to establish the equilibrium phase [24,25]. According to the Al-Ni phase diagram,

* Corresponding author.
E-mail address: deepshikha.s195@gmail.com (D. Shekhawat).

https://doi.org/10.1016/j.jallcom.2024.178026
Received 15 August 2024; Received in revised form 15 November 2024; Accepted 9 December 2024
Available online 10 December 2024

intermetallic compounds such as Al(γ), $NiAl_3$, Ni_2Al_3, NiAl, Ni_5Al_3, Ni_3Al, and Ni(γ) form as Ni concentration increases [25]. The effective heat of formation concept can predict the phase formation sequence [26], where self-sustaining reactions occur if reaction temperature surpasses the melting point of the low-melting component, and the final phase is determined by the Ni-to-Al concentration ratio [23,27,28]. In diffusion couples, the Al_3Ni phase typically forms [29]. When phases with higher melting points form during the heating phase, the formation of concentration-defined phases can be partially or fully suppressed [30,31]. The presence of a two-stage transformation process or melting during initial and reaction product formation affects the reaction propagation velocity and the combustion process's time-temperature profile [32,33]. Factors like porosity, grain size, grain contact dimensions, and powder mixture composition can alter reaction velocity and peak temperature [19,34–39]. In reactive multilayers, variations in bilayer thickness, composition, dilution, and intermixing layer thickness also impact these parameters [1,40]. Maximum reaction temperature is largely determined by the enthalpy of formation of the final product, with secondary transformations, such as melting, potentially modifying it. Reaction velocity is influenced by diffusion distances, diffusion barriers, and impurities at the reactant interfaces [41,42]. In PVD multilayers, these parameters can be finely tuned to control self-propagating reactions [40]. These foils feature nanoscale alternating layers of two elements that react exothermically, with diffusion distances 10–1000 times shorter than in powders, facilitating atomic mixing. Notably, aluminides formed between certain intermetallic compounds do not exhibit large negative heats of mixing and maintain a stable bcc solid solution across a wide concentration range at high temperatures [43]. In such systems, layer thickness influences the heat release during phase formation [43]. Jaekel et al. [44] observed that slower diffusion from thicker Al layers into Ni reduces the overall diffusion rate in reactive multilayers (RML), delaying phase formation. The layering process minimizes porosity and contamination while enhancing contact between reactants compared to powder compacts. Increased packing density accelerates reaction front velocity and system temperature [37,43–45]. Porosity affects thermal conductivity, preheating zone length, temperature distribution, and propagation velocities [37]. Porosity (f) is typically defined as the ratio of pore volume (Vp) to total volume (Vt), expressed as $f = Vp/Vt$ [46]. Lower porosity increases particle contacts, improving thermal conductivity and heat transfer in the preheating zone, extending it and shortening the reaction zone.

A significant increase in the length of the preheating zone leads to greater heat loss, which is necessary in the reaction zone to ensure uniform propagation of the combustion wave. In [37], it is reported that the propagation speed for a sample with 5 % porosity is slower than for a sample with 10 % porosity, which is due to the fact that the lower porosity can lead to instabilities in the combustion wave in extreme cases and change the type of combustion. These differences lead to a sharp increase in reaction rates and enable self-propagation of exothermic reactions in multilayer systems which is not possible in powder compacts. One of the most widely used reactive multilayer systems are Ni/Al multilayers. Al and Ni are easily available, comparatively inexpensive, and have a relatively high reaction enthalpy (1381 J/g) [47]. Fig. 1 shows such a Ni (20 nm)/Al (30 nm) multilayer stack deposited by PVD to a total thickness of 5 μm on a 1 μm thick SiO_2/Si (100) substrate.

These are very useful for reactive bonding as a self-heating source between the substrates to be bonded. Therefore, these bonding techniques have recently increased in the integrated reactive multilayer systems (iRMS) in microelectronics and micromechanical systems (MEMS) [48–53]. Conventional free-standing reactive multilayer films are used in reactive bonding interface technology, which is not practical in micrometer-scale reactive bonding due to the difficulties in handling, positioning and patterning the films. Therefore, integration processing by the patterning/deposition or deposition/patterning of reactive layer system directly on silicon or other substrate components represents an

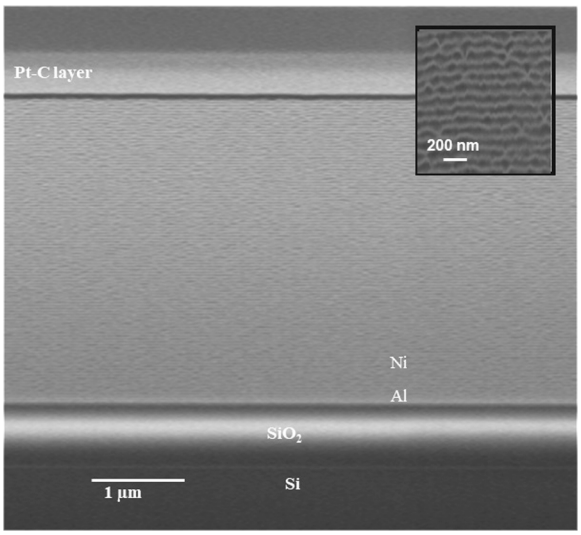

Fig. 1. Scanning microscopy (SEM) image of a focused ion beam (FIB) cross section of fabricated 5 μm Ni/Al multilayer foil with 1:1 Ni/Al atomic ratio (20 nm Ni/30 nm Al) on top of 1 μm SiO_2/Si (100) substrate to be ignited with electric spark and cover with Pt-C layer for FIB cut.

interesting research challenge. In reactive bonding, a highly reactive nanoscale reactive multilayer system is used as a self-heating source between the substrates to be bonded. The heat generation after the external ignition is achieved by a self-propagating exothermic reaction of the integrated reactive multilayers system [51,53–55]. The integrated reactive bond induces localized heat at the bond interface; such limited temperature and velocity, quench locally through the substrate material. This enables bonding through temperature-sensitive microdevices located outside the interface and materials that can be bonded without thermal damage.

In this work, we investigate the effect of the different sizes of the obstacles on the reaction pathway in reactive Ni/Al multilayers on SiO_2/Si substrates. As reactive Ni/Al multilayer films self-ignite spontaneously upon exposure to an external source, they exhibit highly exothermic reactivity. It was also observed that the thermal conductivity of the environment, the strongly limited heat generated at high temperature caused the reaction to spread explosively and in an isotropic direction of propagation. In joining technology, it is necessary to direct the reaction to certain functional points without exceeding critical values of heat release. To meet the requirements and overcome these problems, we attempted to control the reactivity of the reactant with an optimized reaction front velocity and maximum temperature, which affects the dynamics of reaction propagation, and for MEMS [56] applications to design the size and density of obstacles to the propagation of thermal interaction.

2. Materials and experimental techniques

Structured reactive Ni/Al multilayers were prepared on a p-Type Boron doped (100) Silicon substrate (525 μm thick) with a specific resistance of 5 mΩ cm covered with a 1 μm thick SiO_2 layer. First, the substrates were cleaned and spin-coated with AZ 15nxt negative resist of 10 μm thickness. They were then baked on a hot plate at 110 °C for 3 min to allow patterning and the fabrication of square holes of different size. The patterns were produced using the Maskless aligner 150 (MLA 150) machine. The device is equipped with a laser diode source that emits at 405 nm. Exposure was at 340 mJ/cm^2. We fabricated a series of square holes in the 5 μm Ni/Al path with a length of 10, 40, and 100 μm. After exposure, the layer was post baked at 120 °C for 2 min. The patterned geometry was created by dissolving the photoresist with MIF 726 and subsequent metal deposition. Two types of batches were

fabricated. Type A, in which only Ni and Al were deposited and Type B, in which 50 nm Sn was added as an adhesive layer to increase the adhesion of the Ni/Al multilayers after the reaction. Sn-rich solders are commonly used as solder joints in advanced electronic packaging due to their low melting points (210–220 °C) and good wettability [57]. Fig. 2 illustrates the schematic representation of the fabricated design, along with a summary of the fabricated chips. The design features distinct spaces between them, with a column of square-shaped holes spaced 500 μm apart in the x-direction. However, in the y-direction, the distances between holes vary after every two columns, with intervals of 5000, 1000, 500, 300, and so forth, as depicted in the summary provided in Fig. 2. Ni, Al and Sn were deposited by direct current (DC) magnetron sputtering (CS400 by von Ardenne), using Ni, Al and Sn (99.99 % purity, FHR) with 100 mm diameter targets. Alternating layers of Ni and Al with a thickness of 5 μm of Ni/Al multilayers with a thickness of 20 nm Ni and 30 nm Al (50 nm bilayer thickness) were deposited at room temperature. The substrate holder was not provided with active substrate cooling in this system. The depositions were carried out at room temperature and a base pressure of 5×10^{-8} Torr. In general, such deposition conditions promote the formation of nanograins in a columnar structure, which is mainly controlled by the reduced atomic mobility of the deposited materials on the substrate and self-shadowing during film growth [58,59]. After deposition, the resist was removed from the substrate by means of the lift-off process using MLO07 solution. Finally, a series of squares of different sizes were fabricated on SiO_2/Si substrate as shown in Fig. 3. Flow diagram 1 shows the process flow for chip preparation.

An electrical spark of 16 V was used to ignite the reactive multilayers. The electrical probes were placed at the edge of the fabricated chip as schematically depicted in Fig. 2. A high-speed camera (FASTCAM SA-X2) with a frame rate of 50,000 frames per second was used to record the front velocity of the self-propagating reaction. The net velocity of the propagating front was measured by Image J software using manual tracking [60]. The high-speed pyrometer (KLEIBER—Pyroscope 840 pyrometer) was used to measure the reaction temperature with an emissions coefficient (ε) fixed at 1 with a resolution time of 10 μs and 2.2 μm spatial resolution spot on the sample surface where temperature was measured. To investigate the microstructural features on the top of the deposited reactive Ni/Al multilayers on SiO_2/Si substrates, a SEM (S-4800 HITACHI) was used before and after the reaction. Focused ion beam (FIB) nanomilling (Auriga 60, Zeiss) was used to examine the cross-section of the multilayers and record the cross-sections with the integrated scanning electron microscopy (SEM). The operating voltage was set to 5 kV for both cases. Phase analysis by X-ray diffraction (XRD) was performed before and after ignition using the Bruker D5000 theta-theta x-ray diffractometer was used with a Cu Kα (λ = 0.15418 nm) equipped radiation source at 40 mA and 40 kV in Bragg–Brentano mode with a scan speed of 1 s per step and 0.02° step size for 20–100° 2θ angle. The Bruker Diffraction EVA software tool was used to identify the formed phases [61]. Auger spectroscopy was done using an AES Microlab 350 from Thermo Fisher Scientific, Inc. (USA).

3. Results and discussion

3.1. Phase formation and morphology

3.1.1. Before reaction

Fig. 4 shows the XRD patterns of Type A and Type B samples in the as deposited state. It shows the presence of Al (PDF 04-0787) and Ni (PDF 65-2865), Si (PDF 03-0549) and Sn (PDF 65-0298) but no intermetallic phase between Ni and Al. Crystallite and lattice strain were analysed based on the broadening of XRD peaks using the Williamson–Hall (WH) method [62]. According to the WH method, different contributions to the broadening of the reflections are associated with both size and lattice strain effects as follows [62]:

$$\beta \cos\theta = \frac{k\lambda}{D} + 4\varepsilon \sin\theta \quad (1)$$

where, β, θ, k, λ, D and ε are the FWHM, Bragg's angle, shape coefficient (0.98), wavelength (1.54 Å), crystallite size and effective strain respectively.

According to Eq. (1), the strain value is calculated by plotting the curve between β cosθ and sinθ (WH plot), where the slope of the line obtained represents the strain value (ε) and the intersection point represents the crystallite size (D). The measured strain of Ni and Al as well as Sn in the case of type B samples. Since the XRD measurement was performed on the Bragg-Brentano plane, the measured strain is out of plain. A negative slope of the WH plot indicates an effective compressive stress in the crystal lattice [63].

Fig. 5 shows that the crystallite sizes decrease with increasing hole size, which is consistent with the observed SEM images of the top view of Type A and Type B samples shown in Fig. 6. This could be due to the

Summary of the design

No. of columns with similar design	In x direction distance between holes (μm)	In y direction distance between holes (μm)
2	500	5000
2	500	1000
2	500	500
2	500	300
2	500	200
2	500	100
2	500	80
2	500	50
2	500	40
2	500	30
2	500	20
2	500	10

Fabricated design

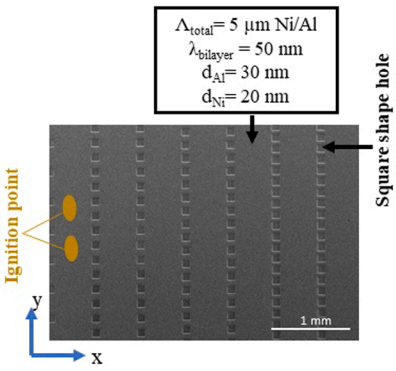

Prepared samples:

Hole size	Type A Λ_{total}= 5 μm Ni/Al	Type B Λ_{total}= 5 μm Ni/Al with 50 nm Sn
	Structured AlNi / SiO_2 (1 μm) / Si (525 μm)	Structured AlNi / Sn (50 nm) / SiO_2 (1 μm) / Si (525 μm)
10 μm	√	√
40 μm	√	√
100 μm	√	√

Fig. 2. SEM image of the fabricated chip of 100 μm hole size sample of Type A layer system, together with summary of the design in tabular form to describes the pattern of holes in the fabricated chip. Prepared samples for ignition experiment, two Types of batches were prepared i.e. Type A is patterned Ni/Al multilayers on SiO_2/Si substrate and whereas Type B prepared patterned Ni/Al multilayers together with 50 nm Sn layer on SiO_2/Si substrate.

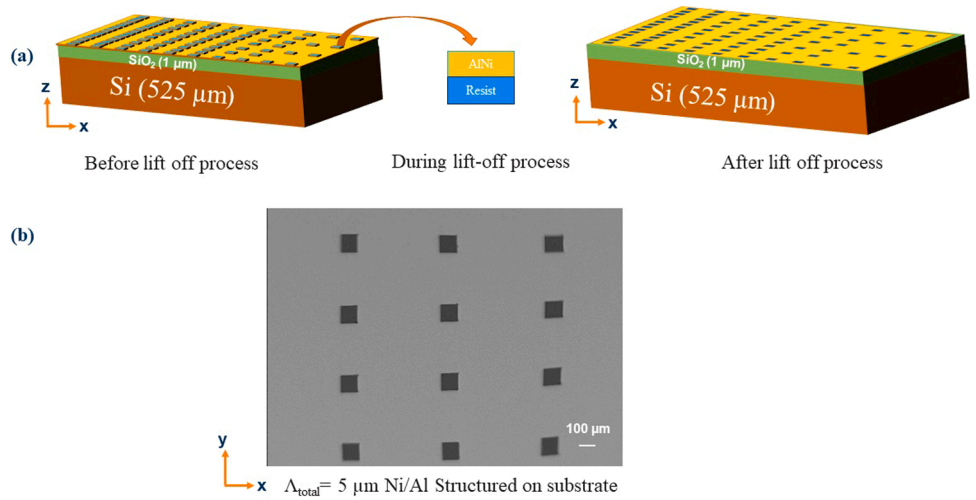

Fig. 3. (a) Process flow: during the Al/Ni multilayers deposition before the lift-off process, and after lift-off and resist removing process. (b) SEM image of the fabricated design of 100 μm side length of holes of Type A sample with Al/Ni multilayer.

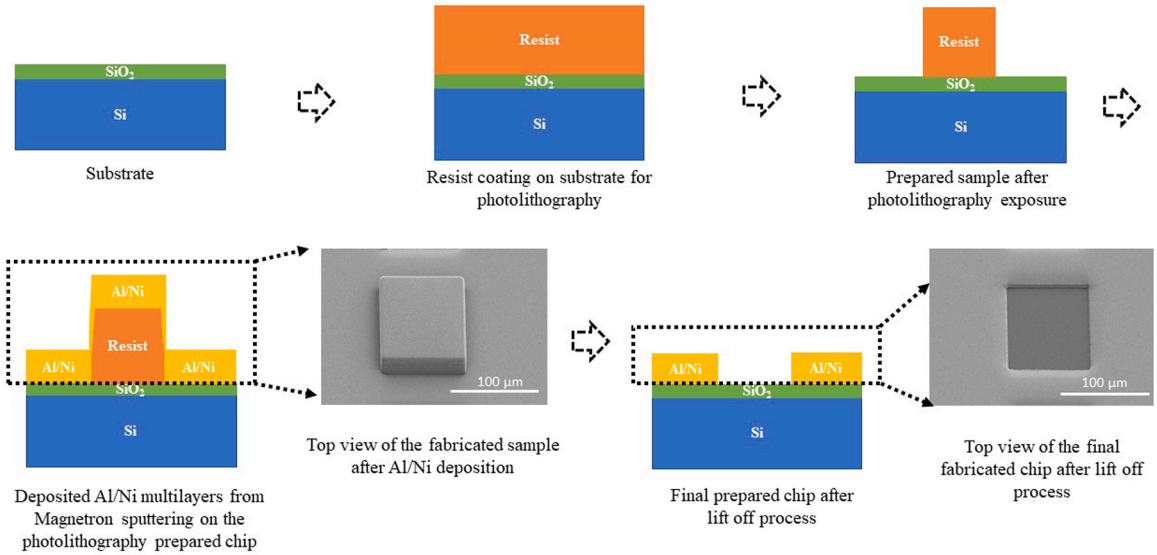

Flow Diagram 1. Process flow for the sample preparation.

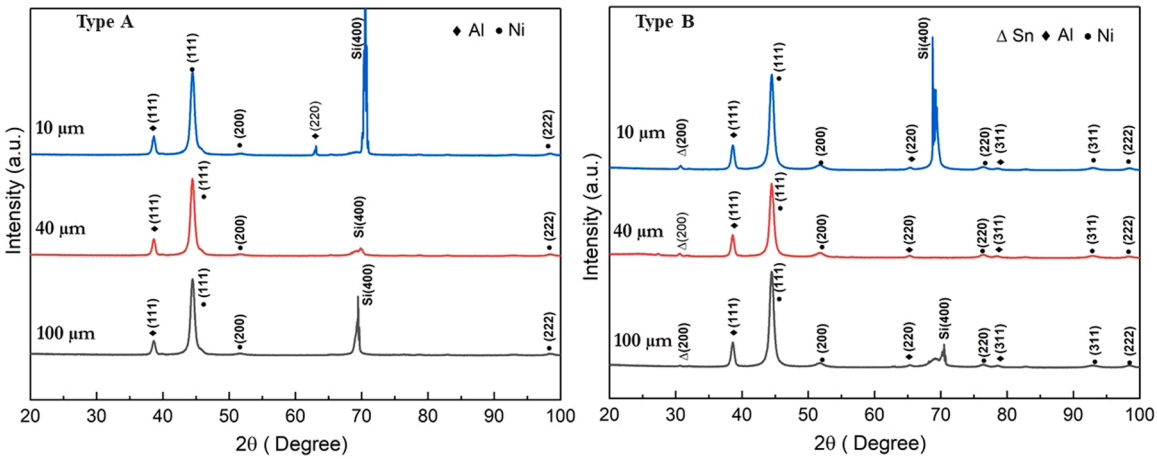

Fig. 4. XRD patterns as deposited Al/Ni multilayers of Type A and Type B samples.

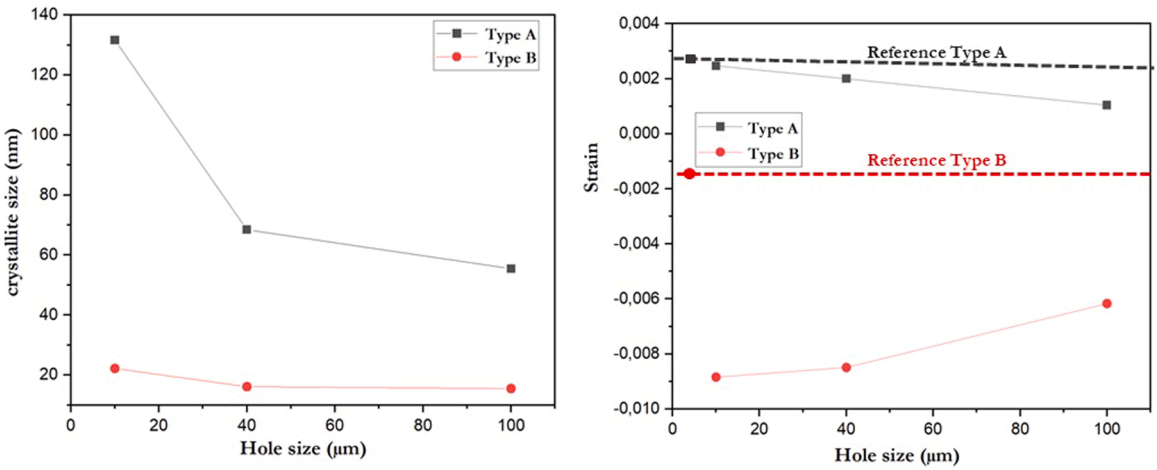

Fig. 5. Variation of crystallite size and strain value with hole size before reaction initiation (as deposited Ni/Al multilayer stack).

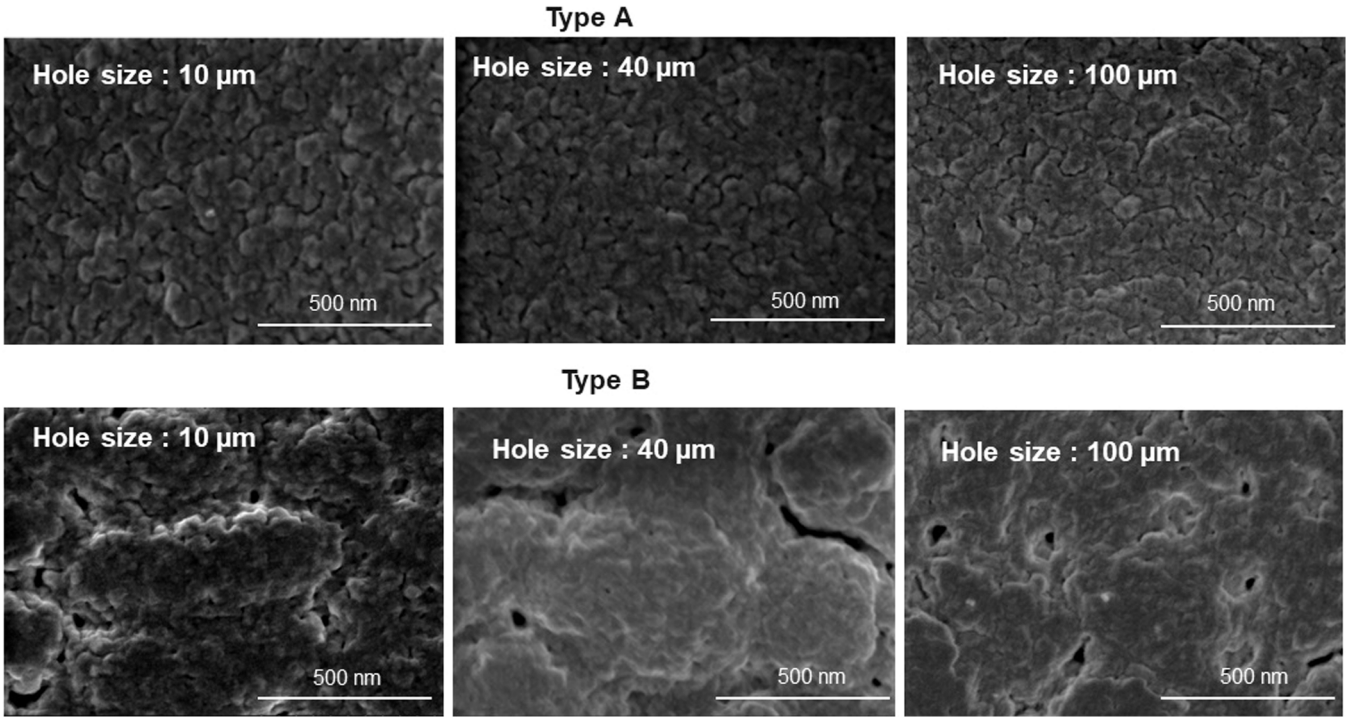

Fig. 6. Top view SEM images of the prepared 10 μm, 40 μm and 100 μm hole size samples of Type A and Type B samples before reaction initiation (as deposited Ni/Al multilayer stack).

deposition conditions of the DC magnetron sputtering tool on the substrates. As we can see in Fig. 3(a), during Ni/Al deposition, the ratio between the area of ion bombardment (yellow part) and the area covered with resist at the location where the holes are formed (black part) decreases as the hole size increases. During the deposition process, the surface of the substrates is bombarded with ions, which increases the local temperature of the substrate surface with deposition. Therefore, we have higher crystallite sizes at a hole size of 10 μm. As the hole size increased, the area of the ion bombardment decreased. As a result, the temperature decreased and a smaller grain size was formed. In addition, the holes do not lead to stresses, but reduce the stresses due to edge relaxation of the deposited reactive multilayers. As the number of holes increases, the contributions of the edges increase, which can lead to a reduction in stress. If it is assumed, that a part of the residual strain arises from the differences in the thermal expansion coefficients a reduced surface temperature reduces also the value of the thermal strain contributing to the residual strain of the layer. As can be seen from the strain values of the samples of reference Type A and reference Type B, the samples without holes are more elongated than the deposited reactive multilayers. However, this applies to the compressive strain of the samples of Type B and the tensile strain of the samples of Type A. It was found that the grain sizes in the Type B samples are smaller than in the Type A samples. This may be due to the presence of Sn. Sn induces compressive strain during deposition [64]. This is the consistent with the observed negative strain value for Type B samples in Fig. 5. introduces compressive strain into the system, which can be understood by the following reasons:

1) Sn act as a wetting layer [65].
2) The deposition of Sn on the SiO_2 layer leads to a deformation or defect at the interface with the substrate. As a result, it leads to roughness of the Al/Ni layers [66,67].

3) The thermal expansion coefficient of Sn is 22 μm/mK, that of Al 25 μm/mK and that of Ni 13 μm/mK [68]. Sn is therefore subjected to compressive stress, while the Al layer is subjected to tensile stress. Consequently, Sn leads to defects and contributes to the buckling effect on the deposited layers, as can be seen in Fig. 7 [66].

Fig. 7 shows the cross-section of the sample Type A and Type B, respectively. In Fig. 7, a Pt–C layer was deposited on the top of the surface to protect the reactive multilayers from the effect of Ga ions by the nanomilling process to obtain the cross-sectional images. Fig. 7 Type A; shows the interface of the Ni/Al multilayers with the substrates is much smoother than that of Type B, where Type B has some defects at the interface of the Ni/Al multilayers with the substrates. The defects and the buckling effect are due to the Sn layer.

3.1.2. After reaction

Fig. 8 shows the XRD patterns of the reacted structured Ni/Al multilayers of Type A and Type B. The Type A case shows the presence of an Al (PDF 04-0787) peak together with the B2 phase NiAl (PDF 65-5171) phase. The Type B case shows the phase formation of B2 phase NiAl (PDF 65-5171), which is consistent with the targeted ratio of $Ni_{50}Al_{50}$ by the deposition along with Ni_3Sn_4 phase (PDF 65-4310) which shows the intermetallic compound formation of Ni_3Sn_4 after the reaction. This phase can be formed as a result of reactive diffusion between Ni and Sn [69] is a stable phase in the Ni-Sn binary phase diagram [70] and can be formed by a peritectic reaction [71,72].

As shown in Fig. 8 for Type A, the presence of Al(111) appeared with lower intensity, indicating that only a small, scattered amount of such unreacted residue is present, resulting from the incomplete reaction of the first deposited Al layer [73].

Fig. 9(a) shows a top-view of the surface morphology of a reacted Ni/Al 100 μm Type A sample. The reacted surface morphology showed a spherulitic-like dendrite or buckling or cracked structures after the reaction [74]. These dendrite orientations were found to emanate from an origin and extend in the direction of propagation of the reaction front to form a sheet-like pattern. The appearance of the dendritic form from the reaction product is a common solid crystallization growth from the molten layer under a rapid-cooling rate [75,76]. The steep temperature gradients that are, systemically known behind the propagation of the reaction front. It would spontaneously induce significant thermal stress gradients related to the solidification process [77]. In addition, the thermal stress states could also increase more if the thermal expansion coefficients of the double-section materials were significantly different [1,78]. These factors contributed to increased stress levels, making the reacted product more susceptible to disintegration or cracking as a result of these associated stresses. It should be noted here that the self-propagating reaction was triggered by the electric current, which occurs explosively and detaches the reacted product in the form of debris particles or flakes, forming interdendritic areas or cracked structures, as shown in Fig. 9(a).

After the reaction, the variation of the grain size observed using FIB cut on the reacted Type A and Type B samples. From Fig. 9(b) and (c), shows the change in the grain size between Type A and Type B samples. Fig. 9(c), also shows the presence of holes or defect on the reacted foil which comes from the pre-existing defect on the Type B samples. The larger grain size observed in Type B than Type A samples. This is due to the fact that Sn increases the thermal resistance in the substrates. Therefore, the addition of Sn decreases the heat losses through the substrates and consequently decreases the cooling rate and increases the maximum temperature and velocity of the type B samples compared to the type A samples. The growth of crystals and grains is strongly dependent on the individual cooling rate [79]. Figs. 10 and 11 shows the time temperature profiles of samples Type A and Type B and the variation of the cooling rate of the respective samples.

Fig. 10 shows the time temperature profile for the samples and shows the different maximum temperature (T_{max}) curves are similar in duration and shape. The emissivity coefficient of the pyrometer was initially set to $\varepsilon = 1$ to emulate an ideal blackbody radiation emitter. However, it's important to note that this property does not accurately reflect the behavior of the Al/Ni RMS, resulting in measured temperatures consistently lower than the actual values [80]. We have since rectified this discrepancy by incorporating the corrected emissivity coefficient values into the measured pyrometer temperature as described in [81]. As shown in the Fig. 10, the time to peak temperature is approximately 0.27 and 21.74 ms; with corresponding heating rates of 3.29 K/μs and 0.049 K/μs for 40 μm Type A and Type B samples respectively as shown in Fig. 10. The cooling rate was recorded as 0.018 K/μs and 0.0039 K/μs in Fig. 10, respectively. The differences in the cooling rate of the samples Type A and B stem from the higher thermal resistance of the sample Type B due to the insertion of the Sn layer. The most important parameters for crystallization and combustion correspond to the magnitude of heating and cooling rate. As can be seen from Fig. 11, the cooling rate increases with the hole size. This can be explained by the available area of Ni/Al materials to be reacted, which induces heat and heat loss through the surrounding, which play an important role in the duration of the forward movement of the reaction front. The cooling rate increases with the hole size as the induced heat is dissipated into the surrounding materials (open holes), which take longer to cool down the temperature after the reaction, which promotes grain growth [79,82]. Therefore, the grain size increased with the decreasing of the cooling rate of the respective materials as shown in Fig. 9(a) and (b).

3.2. Reaction propagation

Fig. 12 shows the characteristic development of the propagation front of the reaction in the 100 μm sample of Type B sample. It shows the successive images of the propagation front taken during the reaction propagation (See Supplementary Video S1 for more details). Fig. 12 (e) and (f) also included the magnified view which was taken by the high-speed camera at 100,000 fps to get the information about the stopping of the reaction front (See Supplementary Video S2 for more details). The mean value of the propagation front velocity and the maximum

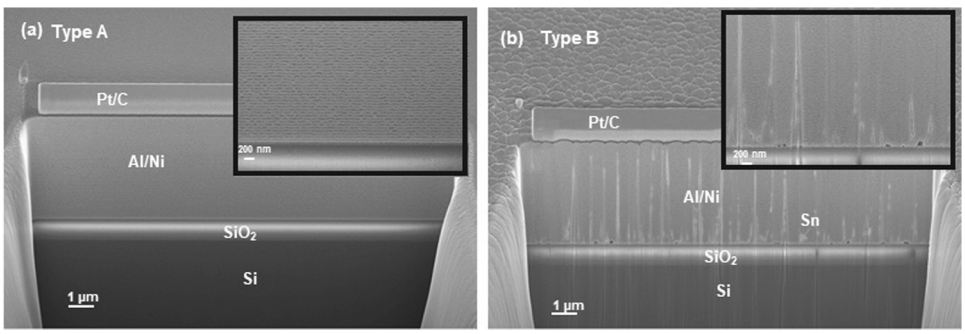

Fig. 7. Cross-sectional FIB image of Type A and Type B samples before reaction.

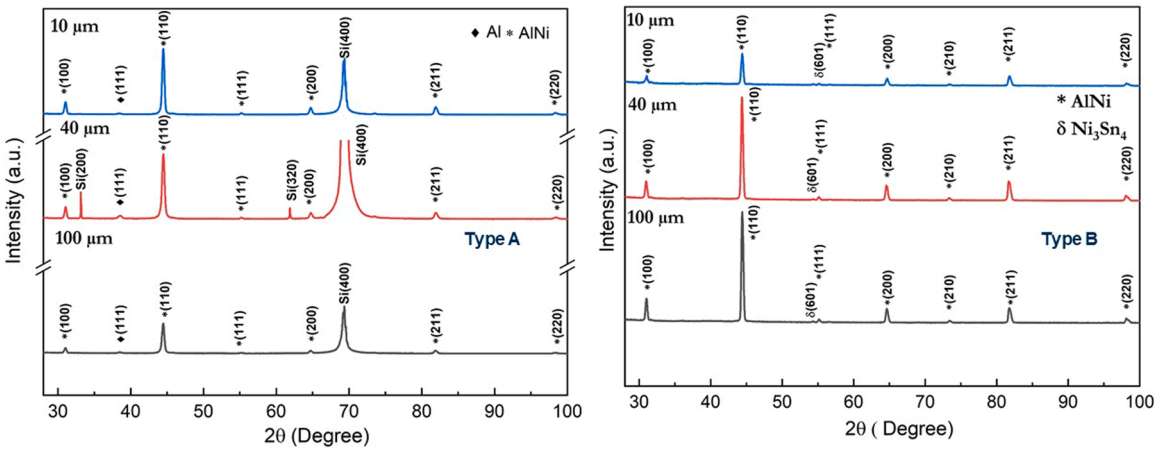

Fig. 8. XRD patterns of the reacted Ni/Al multilayers of Type A and Type B samples.

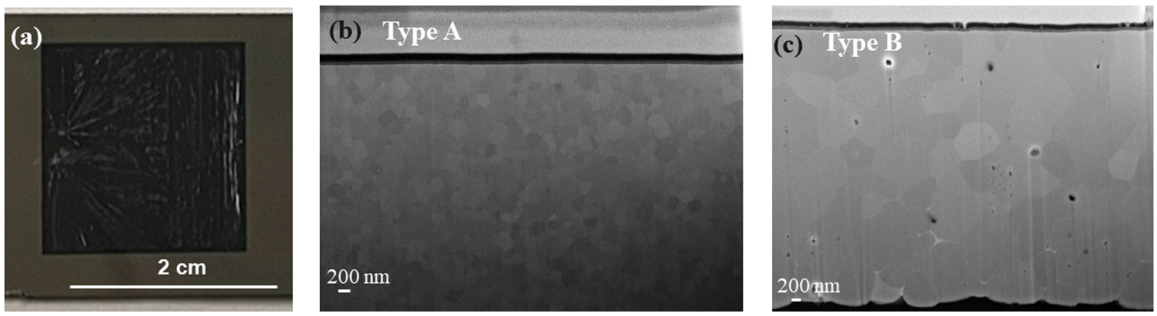

Fig. 9. (a) Photographic image of 2 × 2 cm^2 size chip of 100 μm hole size sample of Type A sample after ignition and reaction completion. (b) and (c) are cross section images prepared with FIB cut of the reacted 10 μm hole size sample of Type A and 10 μm hole size sample of Type B to demonstrate the variation in the grain size after the reaction in Al/Ni multilayers.

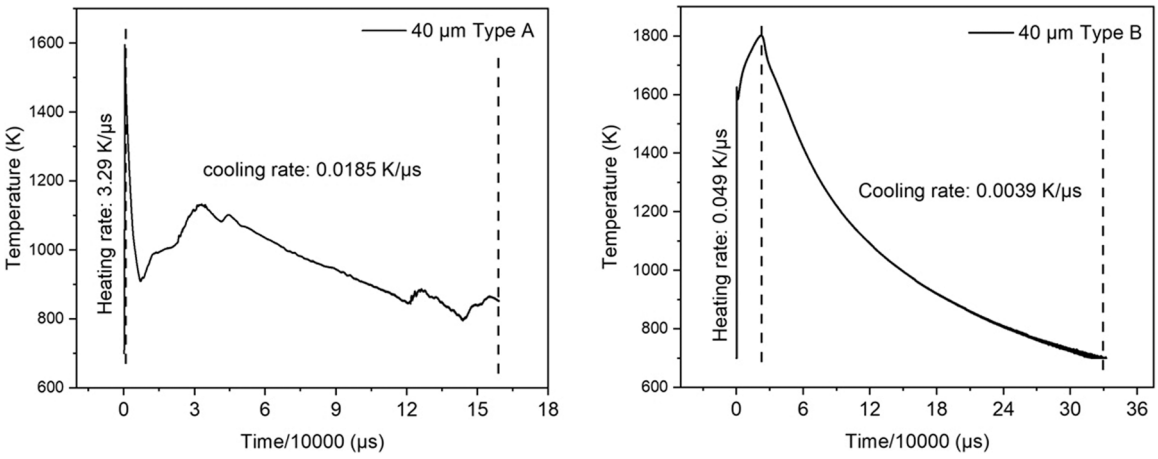

Fig. 10. Time-Temperature dependence and maximum reaction temperature of 40 μm hole size sample of Type A and Type B.

temperature (T_{max}) are shown in the Fig. 13. The front velocity and T_{max} data were collected from 5 samples of every hole size sample sets.

The orange line in Fig. 12 (a) and (b) shows the measured direction of reaction propagation towards the higher concentration of the holes and before the stopping of the front. The self-propagating reaction was initiated on the side of the chip where the largest period of the row of square holes was present (orange arrow in Fig. 12 (a)). In a certain row, the reaction front stopped, the distance between the hole scaled with the hole square size. In Fig. 14, the critical distance for a side length of the square hole of 10 μm was 30 μm, while the critical distance for a side length of the square hole of 100 μm was 50 μm, i.e. longer confinement channels in the hole part of the reactive multilayer on a substrate are causing quenching of the reaction earlier. After the quenching of the self-propagating reaction perpendicular to the rows, a guided self-propagation reaction was observed between two square hole rows. This self-propagating reaction along the rows of holes appeared because there is a frame of a certain width around the rows on the chip. In this frame, the reaction propagates independently of the geometry of the rows of the holes. In Fig. 12 (c) the reaction front stopped, whereas in Fig. 12 (d) further, the reaction front moved upward. Fig. 12 (d)

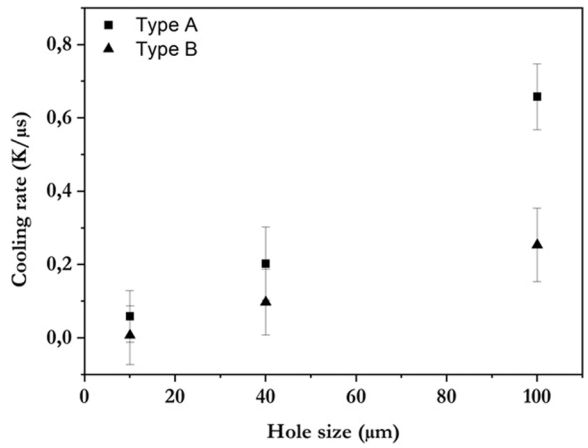

Fig. 11. The variation of cooling rate on hole size of samples of Type A and Type B.

demonstrates the mechanical damage, it happened due to the lattice contraction after the reaction in Ni/Al multilayers [82].

The characteristic velocity and maximum temperature are influenced by the heat loss through the substrates [83–87]. In general, the heat loss is increased by an inert component, i.e. the role of the inert element here is played by the hole, which is not involved in the generation of exothermic reaction. Moreover, the inert element does not contribute to heat generation. As we can observe, the unreacted component is higher for samples with a hole size of 100 μm than for samples with a size of 10 μm, which additionally contributes to a lower heat generation. Therefore, in Fig. 13, the observed velocity of the reaction front and the observed maximum temperature decrease from 10 μm hole size to 100 μm.

Fig. 13 shows the variation of the velocity and temperature with the samples. It can be seen that the velocity and maximum reaction temperature decreases from 10 μm to 100 μm hole sizes. Due to a strongly exothermic reaction of the reactive materials, a self-propagating reaction can be observed, where the heat released by local mixing should be high enough to heat the adjacent material than the heat loss to the surrounding area [83–88]. Therefore, heat loss to the surrounding can influence the velocity of the propagation front by the following way [84]:

$$v = \frac{2\sqrt{\lambda_B}}{\rho_r C_r}\sqrt{Q\frac{\rho_{solid}E_a\tilde{A}}{RT^2} - 16a\sigma T^3} \quad (2)$$

$$\rho_r = \rho_B + \rho_C + \rho_D \quad (3)$$

B, C and D are reaction components, ρ is the density, where $C_r = (\rho_B c_B + \rho_C c_C + \rho_D c_D)/\rho_r$, where C_i is the specific heat of component i, Q is the heat of reaction, T is the initial temperature, σ is the Stefan–Boltzmann constant, a is the mean absorption coefficient. *v* shows the velocity, λ_B the thermal conductivity of component B, ρ_r and ρ_{solid} are the fuel density, R the gas constant 8.314 J (mol K)$^{-1}$ and E_a the activation energy, where 3.1 × 10^4 cal mol^{-1} is recommended value and Ã

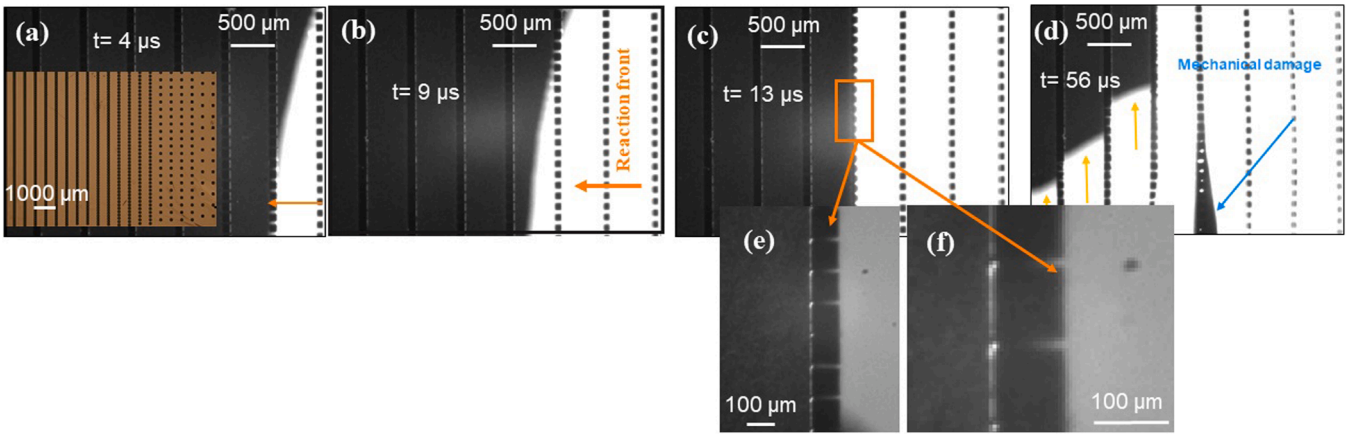

Fig. 12. Time dependent high-speed camera images of the observed reaction propagation front of 100 μm hole size sample Type B: (a) 4 μs, (b) 9 μs, (c) 13 μs, (d) 56 μs. The time is given with respect to the ignition time t = 0 μs.

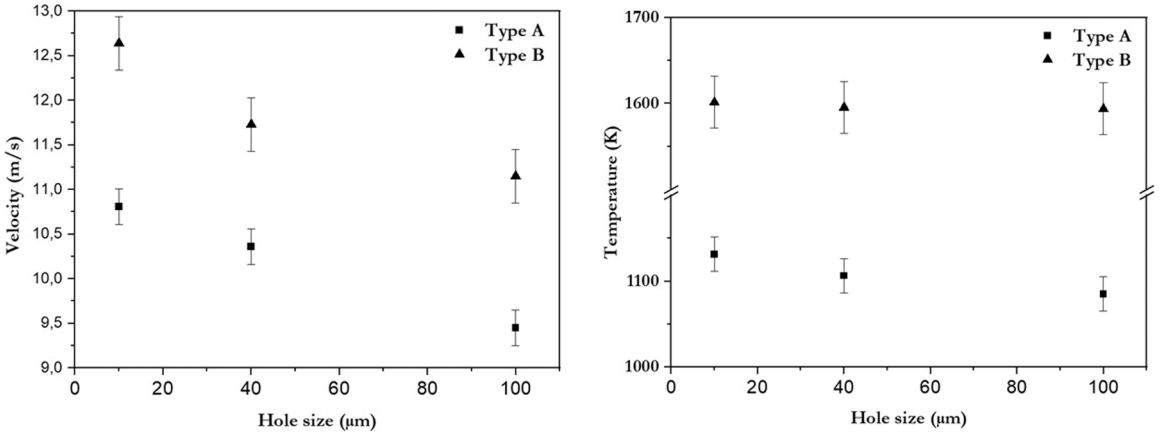

Fig. 13. The variation of the reaction propagation velocity (a) and maximum temperature (b) with hole size of the samples Type A and B.

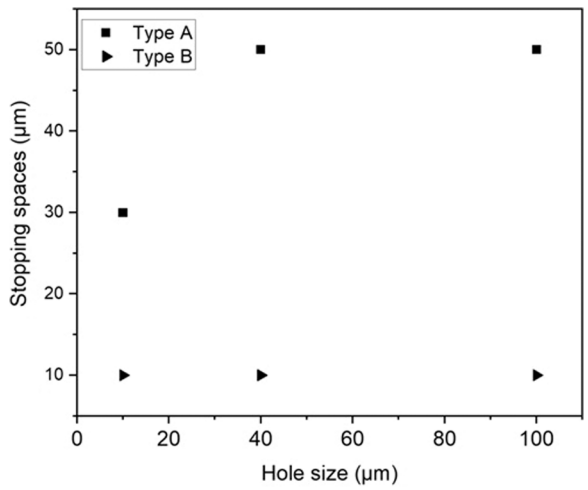

Fig. 14. The variation between observed stopping spaces between holes (distance between holes causing reaction quenching) and hole size in the reactive Ni/Al multilayer.

denotes pre-exponential factor. In Eq. (2), $16a\sigma T^3$ is the heat loss term

From Eq. (2), we can summaries that the reaction front velocity decreases with increasing heat loss. As can be seen in Fig. 12, the reaction front stops between the holes. This stopping space varies with the samples design and thermal properties. Fig. 14 shows the variation between stopping spaces and the different hole sizes of the samples. As we can see, the stopping spaces increase with the hole size. Billingham and Mercer reported that the reaction front is quenched when heat loss parameter (l), $l \geq l_{max} \approx 0.33$ [87]. Therefore, for Type A with 100 μm hole size, the heat generated by the reactive materials is not large enough to exceed the heat loss factor of 0.33. Therefore, the reaction front was quenched. Consequently, this space decreased in the case of a sample with 10 μm hole size. In our particular case, this heat loss factor takes into account the reduced heat generation of the passive hole areas, i.e the cross/section area of the final fabricated sample after list off as shown by schematic in the Flow diagram 1. So, we can conclude that (1) the filling of the cross section (schematic of final fabricated sample after list off as shown in the Flow diagram 1 with reactive materials where holes are located, heat loss reduces with increasing of the hole size. Resultant, generated heat is smaller than heat loss through the surrounding. (2) From thermodynamic point of view, when heat generation and heat loss are equal in the area of the without filling materials in the cross section than critical spaces between holes should be increased to have reaction front due to the available stored energy in the cross section which reduce the generation of the energy. In the cross section of the Al/Ni layers have holes and reactive materials case than the edges of the holes would contributes into the heat loss. Therefore, generation of the heat and heat loss will be affected.

Fig. 13 shows that the reaction velocity and maximum temperature are higher for Type B samples than Type A. This is due to the presence of Sn. Since in the exothermic self-propagating reaction of reactive Ni/Al multilayers the atomic diffusion is normal (z-direction) to the layer, while the thermal diffusion between Al and Ni is parallel (x- and y-direction) to the layers, Sn plays no role in the diffusion through whole layers [89,90]. This is also confirmed by the AES (Auger) measurement. The AES (Auger) measurement shows the detection of Al and Ni, but no Sn was found in the near surface region of type B samples, indicating that diffusion occurs only between Al and Ni. Nevertheless, the Sn wetting layer interacts with the Ni/Al bilayers in contact forming Ni_3Sn_4 as evidenced by X-ray diffraction (see Fig. 8). Sn increases the thermal resistance in the substrates. Therefore, the addition of a Sn layer reduces the heat losses through the substrates and consequently increases the maximum temperature and velocity of the type B samples compared to the type A samples.

4. Conclusion

In the present work, the control of the reaction pathway in reactive Ni/Al multilayers at controlled temperature and velocity mode is demonstrated. We address the complications of heat control around the structured Ni/Al reactive system. We have successfully pattered the reactive Ni/Al multilayers on SiO_2/Si substrates with a systematic network of holes using lift-off technology. The critical feature size was 10 μm. This local modulation of heat loss and heat generation in the multilayer Ni/Al foil reduces the maximum temperature and the propagation velocity. When the periodicity of the holes in a row reaches a certain critical distance, which depends on the size of the geometrically shaped holes, the propagation of the reaction through the row of holes is quenched. Therefore, hole rows with a period smaller than the critical period can be used to control the reaction propagation between them. Furthermore, the reaction ignition in the structured Ni/Al multilayer showed a stable self-sustained propagating reaction front until reach its critical point for the heat loss where reaction quenched. Therefore, it concluded that: (I) The minimum spaces between obstacles can quench/stop the progression of the reaction front; (II) The choice of substrate affects heat dissipation and consequently impacts the advancement of the reaction front; (III) The reaction front can be guided between obstacle rows of obstacles with a specific dimension. (IV) The presence of Sn as an adhesive layer can induce compressive stress during the deposition of the Ni/Al multilayers. This contributes to an increased cooling rate after the reaction and promotes grain growth in the Ni/Al multilayers. Finally, it is observed that the reaction front can be guided between obstacle rows with a certain order of magnitude.

CRediT authorship contribution statement

Joachim Döll: Methodology. **Jörg Pezoldt:** Writing – review & editing, Supervision, Data curation, Conceptualization. **Muhammad Sulman:** Writing – review & editing, Methodology, Investigation. **Deepshikha Shekhawat:** Writing – original draft, Methodology, Investigation, Data curation, Conceptualization. **Dominik Flock:** Writing – review & editing, Investigation, Formal analysis. **Gernot Ecke:** Writing – review & editing, Investigation, Formal analysis. **Marcus Glaser:** Writing – review & editing, Investigation. **Jean Pierre Bergmann:** Writing – review & editing, Investigation.

Declaration of Competing Interest

The authors declare that they have no known competing financial interests or personal relationships that could have appeared to influence the work reported in this paper.

Acknowledgements

The authors express special thanks of gratitude to Sebastian Matthes and Emina Vadro TU Ilmenau, for their help and support for high-speed camera measurement and high-speed pyrometer. Support by the Center of Micro and Nanotechnologies (ZMN), a DFG-funded core facility of TU Ilmenau, is also gratefully acknowledged. The authors acknowledge the financial support of this research by the German Science Foundation under contract numbers PE 624/16-1.

Appendix A. Supporting information

Supplementary data associated with this article can be found in the online version at doi:10.1016/j.jallcom.2024.178026.

Data availability

Data will be made available on request.

References

[1] M.D. Grapes, T.P. Weihs, Exploring the reaction mechanism in self-propagating Al/Ni multilayers by adding inert material, Combust. Flame 172 (2016) 105–115, https://doi.org/10.1016/j.combustflame.2016.07.006.

[2] E.A. Levashov, A.S. Mukasyan, A.S. Rogachev, D.V. Shtansky, Self-propagating high-temperature synthesis of advanced materials and coatings, Int. Mater. Rev. 62 (2017) 203–239, https://doi.org/10.1080/09506608.2016.1243291.

[3] Y. Ivanisenko, A. Mazilkin, I. Gallino, S.S. Riegler, S. Doyle, A. Kilmametov, O. Fabrichnaya, M. Heilmaier, On the formation of nanocrystalline aluminides during high pressure torsion of Al/Ni alternating foils and post-processing multilayer reaction, J. Alloy. Compd. 905 (2022) 164201, https://doi.org/10.1016/j.jallcom.2022.164201.

[4] J. Wang, E. Besnoin, A. Duckham, S.J. Spey, M.E. Reiss, O.M. Knio, M. Powers, M. Whitener, T.P. Weihs, Room-temperature soldering with nanostructured foils, Appl. Phys. Lett. 83 (2003) 3987–3989, https://doi.org/10.1063/1.1623943.

[5] M. Glaser, K. Ehlich, S. Matthes, J. Hildebrand, P. Schaaf, J.P. Bergmann, Influence of metal surface structures on composite formation during polymer–metal joining based on reactive al/ni multilayer foil, Adv. Eng. Mater. (2024) 2302254, https://doi.org/10.1002/adem.202302254.

[6] C.J. Morris, B. Mary, E. Zakar, S.C. Barron, G.M. Fritz, O.M. Knio, T.P. Weihs, R. Hodgin, P. Wilkins, C. May, Rapid initiation of reactions in Al/Ni multilayers with nanoscale layering, J. Phys. Chem. Solids 71 (2010) 84–89, https://doi.org/10.1016/j.jpcs.2009.07.026.

[7] T.W. Barbee, R.L. Simpson, A.E. Gash, J.H. Satcher, Nano-Laminate-based ignitors, Patent US 7.951.247 B2, 2011.

[8] M. Ding, F. Krieger, J. SwankDeveloping nanofoil-heated thin film thermal battery, ARL-TR-6664, U.S. Army Research Laboratory, 2013.

[9] J.-L. Pouchairet, C. Rossi, PyroMEMS as future technological building blocks for advanced microenergetic systems, Micromachines 12 (2021) 118, https://doi.org/10.3390/mi12020118.

[10] C. Rossi, D. Esteve, Micropyrotechnics, a new technology for making energetic microsystems: review and prospective, Sens. Actuators A: Phys. 120 (2005) 297–310, https://doi.org/10.1016/j.sna.2005.01.025.

[11] V.G. Myagkov, L.E. Bykova, S.M. Zharkov, G.N. Bondarenko, Formation of NiAl shape memory alloy films by a solid stat reaction, Sol. St. Phen. 138 (2008) 377–384, https://doi.org/10.4028/www.scientific.net/SSP.138.377.

[12] A.G. Merzhanov, I.P. Borovinskaya, Historical retrospective of SHS: An autoreview, Int. J. Self-Propag. High-Temp. Synth. 17 (2008) 242–265, https://doi.org/10.3103/S1061386208040079.

[13] H.C. Yi, J.J. Moore, Self-propagating high–temperature (combustion) synthesis (SHS) of powder compact materials,, J. Mater. Sci. 25 (1990) 1159–1168, https://doi.org/10.3103/S1061386208040079.

[14] D.P. Adams, Reactive multilayers fabricated by vapor deposition: a crtitical review, Thin Solid Films 576 (2015) 98–128, https://doi.org/10.1016/j.tsf.2014.09.042.

[15] A.S. Rogachev, Reactive multilayer nanofilms: time of scientific and technological maturity, Russ. Chem. Rev. 93 (2024) RCR5106, https://doi.org/10.59761/RCR5106.

[16] A. Wang, S. Maini, J.P. Hickey, J.Z. Wen, Solution synthesis of core-shell n-Al@CuO based on electrostatic self-assembly for enhanced energetic performance, Chem. Eng. J. Adv. 11 (2022) 100323, https://doi.org/10.1016/j.ceja.2022.100323.

[17] Z. Zhuang, K. Xu, B. Liu, Y. Shi, S. Li, Z. Liu, C. He, J. Liu, Improved reactivity and energy release performance of core-shell structured fuel-rich Si/PTFE energetic composites, Combust. Flame 255 (2023) 112889, https://doi.org/10.1016/j.combustflame.2023.112889.

[18] N.A. Isaac, L. Schlag, A. Ispas, J. Reiprich, A.K. Soydan, P.H.O. Moreira, S. Thiele, B. Alibadian, D. Flock, A. Knauer, J.J. Jimenez, A. Bund, F.M. Morales, J. Pezoldt, H.O. Jacobs, Novel gas phase route toward patterned deposition of sputter free Pt/Al nanofoil, Adv. Mater. Technol. 8 (2023) 2300448, https://doi.org/10.1002/admt.202300448.

[19] G.M. Fritz, H. Joress, T.P. Weihs, Enabling and controlling slow reaction velocities in low-density compacts of multilayer reactive particles, Combust. Flame 158 (2011) 1084–1088, https://doi.org/10.1016/j.combustflame.2010.10.008.

[20] L. Battezzati, P. Pappaleopre, F. Durbiano, I. Gallino, Solid state reactions in Al/Ni alternate foils induced by cold rolling and annealing, Acta Mater. 47 (1999) 1901–1914, https://doi.org/10.1016/S1359-6454(99)00040-3.

[21] J.T. Guo, X.H. Du, L.Z. Zhou, Preparation of nanocrystalline NiAl compounds and composites by mechanical alloying, Mater. Sci. Forum 475-479 (2005) 749–754, https://doi.org/10.4028/www.scientific.net/MSF.475-479.749.

[22] S. Sampath, V.P. Ravi, S. Sundararajan, An overview on synthesis, processing and applications of nickel aluminides: from Fundamentals to applications, Crystals 13 (2023) 435, https://doi.org/10.3390/cryst13030435.

[23] K. Kyllesbech Larsen, N. Karpe, J. Bøttiger, Ion irradiation induced phase formation in Al-Ni, J. Mater. Res. 7 (1992) 861–867, https://doi.org/10.1557/JMR.1992.0861.

[24] A.J. Bradley, A. Taylor, An X.ray analysis of the nickel-aluminium system, Proc. R. Soc. Lond. A 159 (1937) 56–72, https://doi.org/10.1098/rspa.1937.0056.

[25] I. Ansara, N. Dupin, H.L. Lukas, B. Sundman, Thermodynamic assessment of the Al-Ni system, J. Alloy. Compd. 247 (1997) 20–30, https://doi.org/10.1016/S0925-8388(96)02652-7.

[26] R. Pretorius, R. De Reus, A.M. Vredenberg, F.W. Saris, Use of the effective heat of formation rule for predicting phase formation sequences in Al-Ni systems, Mater. Lett. 9 (1990) 404–499, https://doi.org/10.1016/0167-577X(90)90094-3.

[27] Yu.S. Naiborodenko, V.,I. Itin, Gasless combustion of mixtures of metal powders: II. Effect of mixture composition on the combustion rate, Combust. Explos. Shock Wave 11 (1975) 626–629, https://doi.org/10.1007/BF00751087.

[28] U. Anselmi-Tamburini, Z.A. Munir, The propagation of solid-state combustion wave in Ni-Al foils, J. Appl. Phys. 66 (1989) 5039–5045, https://doi.org/10.1063/1.343777.

[29] A. Kostka, D. Naujoks, T. Oeller, S. Salomon, E. Öztürk, A. Savan, A. Ludwig, G. Eggeler, Linear growth of reaction layer during in-situ TEM annealing of thin film Al/Ni diffusion couple, J. Alloy. Compd. 922 (2022) 165926, https://doi.org/10.1016/j.jallcom.2022.165926.

[30] T. Neuhauser, G. Tinti, H. Leiste, Casati, M. Stüber, K. Woll, Analysis of the reaction runaway in Al/Ni multilayers with combined nanocalorimetry and time resolved X-ray diffraction, Acta Mater, 195, 2020, pp. 579-587https://doiorg/10.1016/j.actamat.2020.05.035.https://doi.org/10.1016/j.actamat.2020.05.035..

[31] A. Biswas, S.K. Roy, K.R. Gurumurthy, N. Prabhu, S. Banerjee, A Study of self-propagating high-temperature synthesis of NiAl in thermal explosion mode, Acta Mater. 50 (2002) 757–773, https://doi.org/10.1016/S1359-6454(01)00387-1.

[32] I.E. Gunduz, K. Fadenberger, M. Kokonou, C. Rebholz, C.C. Doumanidis, T. Ando, Modelling of the self-propagating reactions of nickel and aluminium multilayer foils, J. Appl. Phys. Lett. 105 (2009) 074903, https://doi.org/10.1063/1.3091284.

[33] S. Besboin, O.M. Cerutti, Knio, Effect of reactant and product melting on self-propagation reactions in multilayer foils, J. Appl. Phys. 92 (2002) 5474–5481, https://doi.org/10.1063/1.1509840.

[34] A.G. Merzhanov, Self-propagating high-temperature synthesis: Twenty years of search and findings, in: Z.A. Munir, J.B. Holt (Eds.), Combustion and Plasma Synthesis of High-Temperature Materials, VCH, New York, 1990, pp. 1–53.

[35] Z.A. Munir, U. Anselmi-Tamburini, Self-propagating exothermic reactions: the synthesis of high-temperature materials by combustion, Mater. Sci. Rep. 3 (1989) 279–365, https://doi.org/10.1016/S0920-2307(89)80002-7.

[36] J. Moore, H.J. Feng, Combustion synthesis of advanced materials: Part I. Reaction parameters, Prog. Mater. Sci. 39 (1995) 243–273, https://doi.org/10.1016/0079-6425(94)00011-5.

[37] H.P. Li, J.A. Sekhar, Numerical analysis for micropyretic synthesis of NiAI intermetallic compound, J. Mater. Sci. 30 (1995) 4628–4636, https://doi.org/10.1007/BF01153072.

[38] H.P. Li, J.A. Sekhar, Numerical analysis for micropyretic synthesis of NiAI intermetallic compound, J. Mater. Sci. 30 (1995) 4628–4636, https://doi.org/10.1007/BF01153072.

[39] H.P. Li, J.A. Sekhar, The influence of the reactant size on the micropyretic synthesis of NiAl intermetallic compounds, J. Mater. Res. 10 (1995) 2471–2480, https://doi.org/10.1557/JMR.1995.2471.

[40] T.P. Weihs, Self-Propagating reactions in multilayer materials, in: D.A. Glocker, S. I. Shah (Eds.), Handbook of Thin Film Process Technology, CRC Press, Bristol, 1998. Chpt. F7.

[41] W.-C. Lee, S.-L. Chung, Ignition phenomena and reaction mechanisms of the self-propagating high-temperature synthesis reaction in the titanium-carbon-aluminum system, J. Am. Ceram. Soc. 80 (1997) 53–61, https://doi.org/10.1111/j.1151-2916.1997.tb02790.x.

[42] E. Ma, M.-A. Nicolet, M. Nathan, $NiAl_3$ formation in Al/Ni thin-film bilayers with and without contamination, J. Appl. Phys. 65 (1989) 2703–2710, https://doi.org/10.1063/1.342756.

[43] C.E. Shuck, A.S. Mukasyan, Reactive Ni/Al nanocomposites: structural characteristics and activation energy, J. Phys. Chem. A 121 (2017) 1175–1181, https://doi.org/10.1021/acs.jpca.6b12314.

[44] J.D. Gibbins, A.K. Stover, N.M. Krywopuska, K. Woll, T.P. Weihs, Properties of reactive Al:Ni compacts fabricated by radial forging of elemental and alloy powders, Combust. Flame (2015) 1–8, https://doi.org/10.1016/j.combustflame.2015.08.003.

[45] D.S. Sundaram, V. Yang, Effect of packing density on flame propagation of nickel-coated aluminum particles, Combust. Flame 161 (2014) 2916–2923, https://doi.org/10.1016/j.combustflame.2014.05.014.

[46] A. Keri, A. Sapi, D. Ungor, D. Sebok, E. Csapo, Z. Konya, G. Galbacs, Porosity determination of nano- and sub-micron particles by single particle inductively coupled plasma mass spectrometry, J. Anal. At. Spectrom. 35 (2020) 1139–1147, https://doi.org/10.1039/D0JA00020E.

[47] S.H. Fischer, M.C. GrubelichA survey of combustible metals, thermites, and intermetallics for pyrotechnic applications, in: Proceedings of the 32nd AIAA/ASME/SAE/ASEE Joint Propulsion Conference Exhibition, American Institute of Aeronautics and Astronautics, Reston, Virigina, 1996, https://doi.org/10.2514/6.1996-3018.

[48] B. Boettge, J. Braeuer, M. Wiemer, M. Petzold, J. Bagdahn, T. Gessner, Fabrication and characterization of reactive nanoscale multilayer systems for low-temperature bonding in microsystem technology, J. Micromech. Microeng. 20 (2010) 064018, https://doi.org/10.1088/0960-1317/20/6/064018.

[49] J. Braeuer, J. Besser, M. Wiemer, T. GessnerRoom-temperature reactive bonding by using nano scale multilayer systems, in: Proceedings of the 2011 16th International Solid-State Sensors, Actuators and Microsystems Conference, Beijing, China, 2011, pp. 1332–1335, http://doi.org/10.1109/TRANSDUCERS.2011.5969498.

[50] X. Qiu, R. Tang, R. Liu, S. Guo, H. YuX. Qiu, R. Tang, R., Liu, S. Guo, H. Yu, A micro initiator realized by reactive Ni/Al nanolaminates for MEMS applications, in:

Proceedings of the 2011 16th International Solid-State Sensors, Actuators and Microsystems Conference, Beijing, China, (2011) 1665–1668, http://doi.org/10.1109/TRANSDUCERS.2011.5969861.
[51] J. Braeuer, J. Besser, M. Wiemer, T. Gessner, Integrated nano scale multilayer systems for reactive bonding in microsystems technology. Proceedings of the 2012 4th Electronic System-Integration Technology Conference, Amsterdam, Netherlands, 2012, pp. 1–4, https://doi.org/10.1109/ESTC.2012.6542144.
[52] J. Braeuer, T. Gessner, A hermetic and room-temperature wafer bonding technique based on integrated reactive multilayer systems, J. Micromech. Microeng. 24 (2014) 115002, https://doi.org/10.1088/0960-1317/24/11/115002.
[53] A. Schumacher, U. Gaiß, S. Knappmann, G. Dietrich, S. Braun, E. Pflug, F. Roscher, K. Vogel, S. Hertel, D. Kähler, W. Reinert, Assembly and packaging of micro systems by using reactive bonding processes. In Proceedings of the 2015 European Microelectronics Packaging Conference (EMPC), Friedrichshafen, Germany, 2015, pp. 1–5.
[54] J. Braeuer, J. Besser, E. Tomoscheit, D. Klimm, S. Anbumani, M. Wiemer, T. Gessner, Investigation of different nano scale energetic material systems for reactive wafer bonding, ECS Trans. 50 (2013) 241–251, https://doi.org/10.1149/05007.0241ecst.
[55] J. Braeuer, J. Besser, M. Wiemer, T. Gessner, A novel technique for MEMS packaging: Reactive bonding with integrated material systems, Sens. Actuators A Phys. 188 (2012) 212–219, https://doi.org/10.1016/j.sna.2012.01.015.
[56] T. Wu, B. Julien, H. Wang, S. Pelloquin, A. Esteve, M. Zachariah, C. Rossi, Engineered porosity-induced burn rate enhancement in dense Al/CuO nanothermites, ACS Appl. Energy Mater. 5 (2022) 2642–3885. ⟨https://laas.hal.science/hal-03584996⟩.
[57] S. He, R. Gao, Yu-An Shen, J. Li, H. Nishikawa, Wettability, interfacial reactions, and impact strength of Sn–3.0Ag–0.5Cu solder/ENIG substrate used for fluxless soldering under formic acid atmosphere, J. Mater. Sci. 55 (2020) 3107–3117, https://doi.org/10.1007/s10853-019-04153-9.
[58] B.A. Movchan, A.V. Demchishin, Structure and properties of thick condensates of nickel, titanium, tungsten, and aluminum oxides, and zirconium dioxide in vacuum, Fiz. Met. Metalloved. 28 (1969) 653–660 (in Russian).
[59] J.A. Thornton, The microstructure of sputter-deposited coatings, J. Vac. Sci. Technol. A 4 (1986) 3059–3065, https://doi.org/10.1116/1.573628.
[60] C.A. Schneider, W. Rasband, K.W. Eliceiri, NIH Image to ImageJ: 25 years of image analysis, Nat. Methods 9 (2012) 671–675, https://doi.org/10.1038/nmeth.2089.
[61] Brucker, Diffrac. EVA.
[62] D.L. Dorset, Book review- X-ray diffraction: a practical approach, Microsc. Microanal. 4 (1999) 513–515, https://doi.org/10.1017/S143192769800049X.
[63] W.M.S. Silva, N.S. Ferreira, J.M. Soares, R.B. da Silva, M.A. Macedo, Investigation of structural and magnetic properties of nanocrystalline Mn-doped $SrFe_{12}O_{19}$ prepared by proteic sol–gel process, J. Magn. Magn. Mater. 395 (2015) 263–270, https://doi.org/10.1016/j.jmmm.2015.07.085.
[64] S. Zhang, H. Hajiyani, A.G. Hufnagel, J. Kampmann, B. Breitbach, T. Bein, D. F. Rohlfing, R. Pentcheva, C. Scheu, Sn-doped hematite for photoelectrochemical water splitting: the effect of Sn concentration, Z. Phys. Chem. 234 (2020) 683–698, https://doi.org/10.1515/zpch-2019-1482.
[65] S. Amore, E. Ricci, G. Borzone, R. Novakovic, Wetting behaviour of lead-free Sn-based alloys on Cu and Ni substrates, Mater. Sci. Eng. A 495 (2008) 108–112, https://doi.org/10.1016/j.msea.2007.10.110.
[66] J. Tupala, M. Kemell, M. Mattinen, Atomic layer deposition of tin oxide thin films from bis[bis(trimethylsilyl) amino] tin (II) with ozone and water, J. Vac. Sci. Technol. A 35 (2017) 041506, https://doi.org/10.1116/1.4984279.
[67] T. Stabile, Y.S. Li, Strained a-Sn thin films on highly lattice-mismatched Ge substrates, Mater. Today Adv. 12 (2021) 100189, https://doi.org/10.1016/j.mtadv.2021.100189.
[68] ⟨https://en.wikipedia.org/wiki/Thermal_expansivities_of_the_elements⟩.
[69] M. Mita, M. Kajihara, N. Kurokawa, N. Sakomoto, Growth behaviour of Ni3Sn4 layer during reactive diffusion between Ni and Sn at solid-state temperatures, Mater. Sci. Eng. A 403 (2005) 269–275, https://doi.org/10.1016/j.msea.2005.05.012.
[70] V. Gandova, Thermodynamic description of Ni based binary phase diagrams, Int. J. Innov. Sci. Eng. Technol. 3 (2016) 161–166.
[71] W. Mikulas, L. Thomassen, Equilibrium relations in the Ni-Sn system, Trans. AIME 124 (1937) 111–137.
[72] C. Schmetterer, H. Flandorfer, K.W. Richter, U. Saeed, M. Kauffman, P. Roussel, H. Ipser, A new imvestigation oft he system Ni-Sn, Intermetallics 15 (2007) 869–884, https://doi.org/10.1016/j.intermet.2006.10.045.
[73] E.-M. Bourim, Il-S. Kang, H.Y. Kim, Investigation of integrated reactive multilayer systems for bonding in microsystem technology, Micromachines 12 (2021) 1272, https://doi.org/10.3390/mi12101272.
[74] A.K. Sinha, Physical Metallurgy Handbook, McGraw-Hill, New York, NY, 2003.
[75] M.E. Glicksman, Principles of Solidification: An Introduction to Modern Casting and Crystal Growth Concepts, Springer, New York, 2011.
[76] A.G. Shtukenberg, Y.O. Punin, E. Gunn, B. Kahr, Spherulites, Chem. Rev. 112 (2012) 1805–1838, https://doi.org/10.1021/cr200297f.
[77] A. Andreadou, J. Pezoldt, Ch Förster, E.K. Polychroniadis, M. Voelskow, W. Skorupa, Buckling stabilization and stress reduction in SiC on Si by i-FLASiC processing, Mater. Sci. 600 (2008) 239–242, https://doi.org/10.4028/www.scientific.net/MSF.600-603.239.
[78] A.S. Rogachev, S.G. Vadchenko, F. Baras, O. Politano, S. Rouvimov, N.V. Sachkova, M.D. Grapes, T.P. Weihs, A.S. Mukasyan, Combustion in reactive multilayer Ni/Al nanofoils: experiments and molecular dynamic simulation, Combust. Flame 166 (2016) 158–169, https://doi.org/10.1016/j.combustflame.2016.01.014.
[79] A.S. Rogachev, S.G. Vadchenko, A.S. Shchukin, SHS reaction and explosive crystallization in thin films: resemblance and distinction, Int. J. Self-Propagating High. -Temp. Synth. 26 (2017) 44–48, https://doi.org/10.3103/S1061386217010095.
[80] S. Matthes, M. Glaser, E. Vardo, Y.H.S. Camposano, K. Jaekel, J.P. Bergmann, P. Schaaf, Influence of extrinsic induced tensile stress on the selfpropagating high-temperature synthesis of nanosized Al/Ni multilayers, J. Mater. Sci. 58 (2023) 10085–10095, https://doi.org/10.1007/s10853-023-08618-w.
[81] ⟨https://mhi-inc.com/basics-of-radiation-power-transfer⟩.
[82] J.C. Trenkle, L.J. Koerner, M.W. Tate, N. Walker, S.M. Gruner, T.P. Weihs, T. C. Hufnagel, Time-resolved x-ray microdiffraction studies of phase transformations during rapidly propagating reactions in Al/Ni and Zr/Ni multilayer foils, J. Appl. Phys. 107 (2010) 113511, https://doi.org/10.1063/1.3428471.
[83] D. Shekhawat, M. Baloochi, D. Sudhahar, V.A. Raheja, J. Döll, H.O. Jacobs, J. Pezoldt, Infuence of environment on self-propagating reactions in Al/Ni multilayer foils, MRS Adv. 8 (2023) 477–483, https://doi.org/10.1557/s43580-023-00574-6.
[84] J. Fort, T. Pujol, A.S. Cukrowski, Several-temperature systems: extended irreversible thermodynamics and thermal wavefront propagation, J. Phys. A: Math. Gen. 33 (2000) 6953–6973, https://doi.org/10.1088/0305-4470/33/39/310.
[85] O.S. Rabinovich, P.S. Grinchuk, M.A. Andreev, B.B. Khina, Conditions for compustion synthesis in nanosized Ni/Al films on a substrate, Phys. B 392 (2007) 272–280, https://doi.org/10.1016/j.physb.2006.11.032.
[86] T.V. Zaporozhets, A.M. Gusak, A.I. Ustinov, Conditions of propagation of the SHS reaction front in nanolayered foils in contact with heat-conducting material, Paton Weld. J. 8 (2011) 37–41.
[87] J. Billingham, G.N. Mercer, The effect of heat loss on the propagation of strongly exothermic combustion waves, Combust. Theory Model. 5 (2001) 319–342, https://doi.org/10.1088/1364-7830/5/3/304.
[88] A.J. Gavens, D. Van Heerden, A.B. Mann, M.E. Reiss, T.P. Weihs, Effect of intermixing on self-propagating exothermic reactions in Al/Ni nanolaminate foils, J. Appl. Phys. 87 (2000) 1255–1263, https://doi.org/10.1063/1.372005.
[89] R.L. Xu, M. Munoz Rojo, S.M. Islam, A. Sood, B. Vareskic, A. Katre, N. Mingo, K. E. Goodson, H.G. Xing, D. Jena, E. Pop, Thermal conductivity of crystalline AlN and the influence of atomic-scale defects, J. Appl. Phys. 126 (2019) 185105, https://doi.org/10.1063/1.5097172.
[90] Y. Yan, S.C. King, M. Li, T. Galy, M. Marszewski, J.S. Kang, L. Pilon, Y. Hu, S. H. Tolbert, Exploring the effect of porous structure on thermal conductivity in templated mesoporous silica films, J. Phys. Chem. C 123 (2019) 21721–21730, https://doi.org/10.1021/acs.jpcc.9b03767.